Simultaneously Efficient Light Absorption and Charge Separation in WO₃/BiVO₄ Core/Shell Nanowire Photoanode for Photoelectrochemical Water Oxidation

Pratap M. Rao,[†,∥,⊥] Lili Cai,[†,⊥] Chong Liu,[‡] In Sun Cho,[†] Chi Hwan Lee,[†] Jeffrey M. Weisse,[†] Peidong Yang,[‡,§] and Xiaolin Zheng*[,†]

[†]Department of Mechanical Engineering, Stanford University, Stanford, California 94305, United States
[‡]Department of Chemistry, University of California, Berkeley, California 94720, United States
[§]Materials Sciences Division, Lawrence Berkeley National Laboratory, Berkeley, California 94720, United States

Ⓢ Supporting Information

ABSTRACT: We report a scalably synthesized WO₃/BiVO₄ core/shell nanowire photoanode in which BiVO₄ is the primary light-absorber and WO₃ acts as an electron conductor. These core/shell nanowires achieve the highest product of light absorption and charge separation efficiencies among BiVO₄-based photoanodes to date and, even without an added catalyst, produce a photocurrent of 3.1 mA/cm² under simulated sunlight and an incident photon-to-current conversion efficiency of ~60% at 300−450 nm, both at a potential of 1.23 V versus RHE.

KEYWORDS: BiVO₄, WO₃, photoelectrochemical, water splitting, photoanode, core/shell nanowire
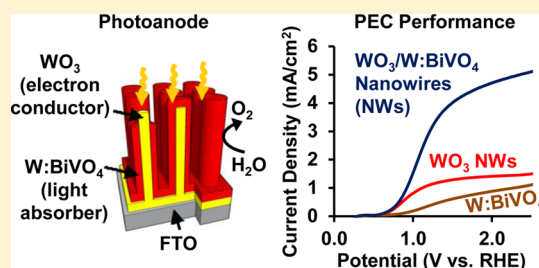
Photoelectrochemical (PEC) water splitting produces hydrogen using solar energy and is an example of artificial photosynthesis, by which the energy of sunlight is converted to chemical fuels.[1,2] Because of the large voltage required for water splitting and the desirability of small band gaps for efficient light absorption, a two-electrode tandem system in which a photocathode and photoanode are connected in series and the water-splitting reaction is divided into two half reactions, promises to be more efficient than a single semiconductor system.[2−5] However, the efficiency of these proposed tandem systems is presently limited by the low photocurrents achieved by the oxygen-evolving photoanodes.[6,7] Because of their stability under oxidizing conditions,[8,9] metal oxides have been heavily researched as materials for the photoanode. However, the commonly studied binary oxides TiO₂[10,11] and WO₃[12] have band gaps that are too large to absorb light efficiently (~3.0 and ~2.6 eV, respectively), while the commonly studied Fe₂O₃, despite its desirable band gap of ~2.2 eV, has a conduction band edge at 0.55 V versus the reversible hydrogen electrode (RHE),[13] which is further from the vacuum level than desired for a PEC photoanode, and extremely poor charge transport properties that have prevented efficient charge separation.[14−16]

Recently, the ternary oxide BiVO₄ has become the top-performer among all metal oxide photoanodes due to its relatively small band gap of 2.4 eV that permits efficient light absorption, its relatively negative conduction band edge (~0 V versus RHE), and moderate charge transport properties.[6,17,18] Theoretically, the maximum water oxidation photocurrent (J_{max}) for BiVO₄ photoanodes under Air-Mass 1.5 Global (AM 1.5G) solar illumination is 7.5 mA/cm².[17] Nevertheless, the

practical water oxidation photocurrent (J_{H_2O}) is much lower due to the limited light absorption, charge separation, and surface charge transfer efficiencies (η_{abs}, η_{sep} and η_{trans}, respectively) of the BiVO₄ material, according to $J_{H_2O} = J_{max} \times \eta_{abs} \times \eta_{sep} \times \eta_{trans}$.[13,19,20] Various efforts have been devoted to increase these efficiencies. Specifically, the charge transfer efficiency η_{trans} has been dramatically improved by coating oxygen evolution reaction (OER) catalysts onto the BiVO₄ surface for improving the water oxidation kinetics and/or passivating surface defects.[6,18,19,21−29] The charge separation efficiency η_{sep} of BiVO₄ has been improved by a range of methods, including introduction of nanoscale porosity,[6,19,21,22,24,26,27,30,31] reduction of BiVO₄ thickness,[6,25] introduction of electron-donating dopants such as Mo and W,[6,19,22,27,32−35] and formation of a distributed homojunction by the introduction of a gradient doping concentration of W in a BiVO₄ film.[18] Moreover, η_{sep} has also been improved by the formation of heterojunctions of BiVO₄ with other materials including films (SnO₂,[18,25,36−38] SiO₂,[39] WO₃,[35,40−42] graphene,[43] and others[44,45]) and nanowires (WO₃[46,47] and Fe₂O₃[48]). Among the latest state-of-the-art BiVO₄-based photoanodes, the highest efficiency was achieved by a W-doped BiVO₄ film with gradient doping of W and an underlying SnO₂ heterojunction, synthesized on a textured substrate, and coated with cobalt phosphate (CoPi) OER catalyst, for which η_{abs}, η_{sep}, and η_{trans} were reported at the reversible water

oxidation potential of 1.23 V versus RHE as 75, 60, and nearly 100%, respectively.[18] Though η_{trans} at 1.23 V versus RHE has approached nearly 100% by the use of OER catalysts, the achieved $\eta_{abs} \times \eta_{sep}$ product is only 45% because the hole and electron diffusion lengths are shorter than the light absorption depth.[6,19,25,37] Hence, achieving simultaneously high η_{abs} and η_{sep} remains a challenge and needs to be addressed in order to realize high performance BiVO$_4$ photoanodes for PEC water oxidation.

In this study, we demonstrate a photoanode that achieves the highest reported $\eta_{abs} \times \eta_{sep}$ product (53%) among BiVO$_4$-based photoanodes by coating a thin layer of BiVO$_4$ onto a vertical array of electrically conductive WO$_3$ nanowires (NWs) to form WO$_3$/W-doped BiVO$_4$ core/shell NWs (WO$_3$/W:BiVO$_4$ NWs, Figure 1a). In this structure, BiVO$_4$ is the primary light
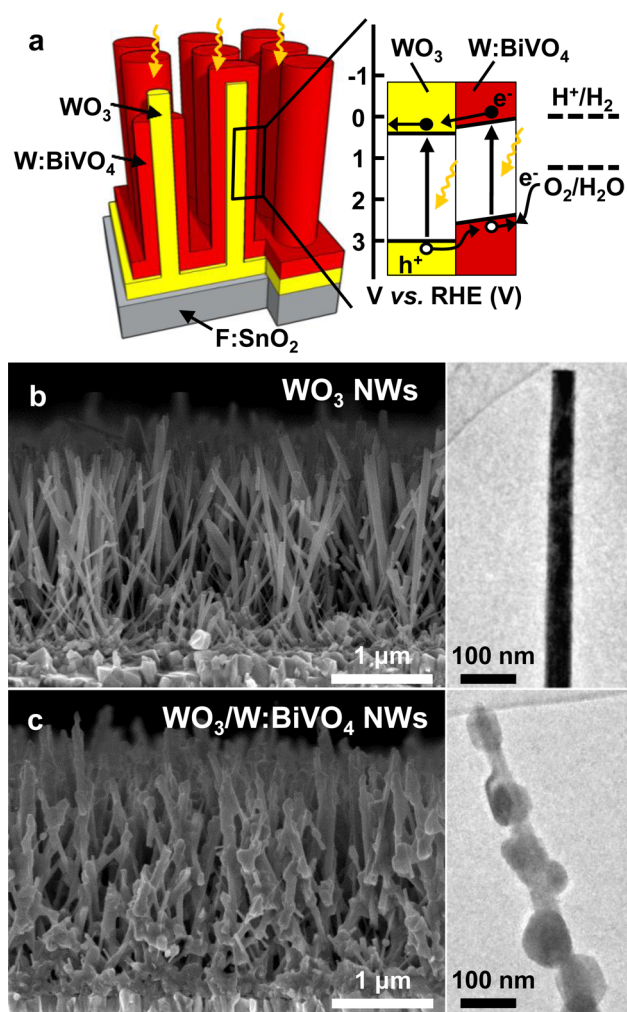

Figure 1. The WO$_3$/W:BiVO$_4$ core/shell nanowire (NW) photoanode. (a) Structural schematic and energy band diagram of the core/shell NWs and type-II staggered heterojunction, in which charges generated in both the W:BiVO$_4$ shells and WO$_3$ NW cores can contribute to the water oxidation photocurrent. The band edges and water oxidation and reduction potentials are plotted on the reversible hydrogen electrode (RHE) scale. (b,c) Scanning electron microscope (SEM, left) and transmission electron microscope (TEM, right) images of the bare WO$_3$ NW array (75 nm average NW diameter) and WO$_3$/W:BiVO$_4$ core/shell NWs (60 nm average W:BiVO$_4$ shell thickness), respectively. The W:BiVO$_4$ shell consists of a single layer of densely packed nanoparticles.

absorber and WO$_3$ acts as an electron conductor. Such core/shell NWs successfully incorporate all the previously mentioned strategies for enhancing charge separation in BiVO$_4$, including thickness reduction, introduction of nanoscale porosity, heterojunction formation, and gradient doping, into a single structure. In addition, they permit efficient light absorption by orthogonalizing the directions of light absorption and charge transport in BiVO$_4$ and further improve charge separation by providing a conductive pathway through the WO$_3$ NW cores for electrons to reach the current collector. Though a WO$_3$/BiVO$_4$ core/shell nanorod photoanode[46] and a WO$_3$ NW/BiVO$_4$ heterojunction photoanode[47] have been attempted before, the efficiency of the present WO$_3$/W:BiVO$_4$ NW photoanodes is higher because of superior morphology which simultaneously optimizes light absorption and charge transport. In the following, we will describe the synthesis and characterization of the present WO$_3$/W:BiVO$_4$ NWs in detail and explain the origin of the improved PEC performance.

The WO$_3$/W:BiVO$_4$ NWs were synthesized by a combination of flame vapor deposition and drop-casting. First, flat fluorine-doped tin oxide (FTO) substrates (2.5 × 1.7 cm, 2.3 mm thick, 8 Ω/□, Hartford Glass) were cleaned and completely coated with a layer of 70−100 nm thick tungsten oxide by spin-coating in order to promote uniform and dense nucleation of the NWs.[49] Next, crystalline substoichiometric W$_{18}$O$_{49}$ NWs were synthesized on the coated FTO substrates via atmospheric flame vapor deposition at a substrate temperature of 550 °C for 30 min, as reported in our previous work.[49−52] This flame-synthesis method is rapid, economical, and scalable, which is important for practical applications. The as-grown W$_{18}$O$_{49}$ NWs were further annealed in air at 550 °C in a box furnace for 2 h, after which stoichiometric WO$_3$ NWs were obtained (Figure 1b). Next, a solution containing 50 mM bismuth and 46.5 mM vanadium prepared by dissolving bismuth nitrate pentahydrate (98%) and vanadyl acetylacetonate (98%) in 20:1 (v/v) acetic acid (99.7%)/acetyl acetone (99%) was coated onto the WO$_3$ NWs by drop-casting. Six coats of the solution in total were applied to each sample. For each coat, 20 μL was dropped on the sample, which was allowed to dry at room temperature and then briefly annealed on a hot plate at 450 °C for 2 min. Finally, after all the coating steps the samples were annealed in air at 550 °C in a box furnace for 2 h to yield a crystalline W-doped BiVO$_4$ shell composed of a single layer of densely packed nanoparticles on the WO$_3$ NWs (Figure 1c). Here, W was naturally doped into BiVO$_4$ during the annealing process because of the intimate contact of WO$_3$ and BiVO$_4$ in the core/shell structure, as will be described next.

The morphologies, crystal structures, and chemical composition of the WO$_3$/W:BiVO$_4$ core/shell NWs were characterized by scanning electron microscopy (SEM, FEI Sirion XL30, 5 kV), parallel beam X-ray diffraction (XRD, PANalyticalXPert 2, Cu-kα, 45 kV, 40 mA), transmission electron microscopy (TEM, FEI Tecnai G2 F20 X-TWIN FEG, 200 kV), and TEM-energy dispersive X-ray spectroscopy (TEM-EDS). Monoclinic WO$_3$ and monoclinic W:BiVO$_4$ are the only phases detected in XRD measurements (Figure 2a). The XRD pattern of the WO$_3$ NWs is nearly unchanged after adding the W:BiVO$_4$ shell and the average W doping in the W:BiVO$_4$ shell is approximately 7%, as estimated from the magnitude of the shift of the W:BiVO$_4$ XRD peaks from those of undoped BiVO$_4$ (Supporting Information Figure S1).[19,32,33] It is known that W^{6+} dopes into BiVO$_4$ by substituting for V^{5+}
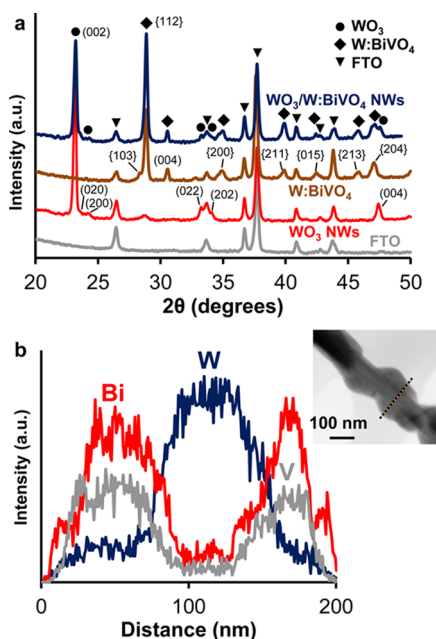
Figure 2. Crystallographic and chemical characterization of the WO_3/W:$BiVO_4$ core/shell NWs and control samples. (a) X-ray diffraction (XRD) patterns of the WO_3/W:$BiVO_4$ NWs, a porous planar W:$BiVO_4$ film containing the same mass of Bi as that in the core–shell NWs (hereafter referred to as the same-mass W:$BiVO_4$ film), the bare WO_3 NWs, and the bare FTO (fluorine-doped tin oxide) substrate, showing that monoclinic WO_3 and monoclinic W:$BiVO_4$ are the only phases present in the WO_3/W:$BiVO_4$ core/shell NWs. The (002) peak of WO_3 is enhanced relative to the (020) and (200) peaks, indicating that the WO_3 NW axis is along the [001] direction of the NW crystals. (b) Results of TEM-energy dispersive X-ray spectroscopy (TEM-EDS) on the WO_3/W:$BiVO_4$ core/shell NW pictured in the inset TEM image, showing the interdiffusion of elements at the interface and gradient doping of W into the $BiVO_4$ shell.

and acts as an electron donor.[32] For this reason, the Bi–V drop-casting solution was formulated to contain Bi:V = 100:93 with 7% W-doping coming from the WO_3 NWs. In addition, the TEM-EDS (Figure 2b) clearly shows that there is considerable interdiffusion of the elements across the core/shell interface, and the sum of the V and W concentrations is approximately equal to the Bi concentration in the shell, as would be expected for W-doped $BiVO_4$. Moreover, there is a concentration gradient of W in the $BiVO_4$ shell, with the highest W concentration near the WO_3 core and decreasing W concentration across the shell. The best-performing photo-anode consists of WO_3 NWs with average lengths of 2.5 μm, average diameters of 75 nm and average interwire spacing of 350 nm, coated with a W:$BiVO_4$ layer of 60 nm average thickness (see Supporting Information Figure S2 and S3 for additional SEM images and a histogram of NW diameters).

The PEC performance of the WO_3/W:$BiVO_4$ core/shell NW photoanode (masked to expose an illuminated area of 0.63 cm^2) was evaluated by measuring the current density–voltage ($J-V$) curve and incident photon-to-current conversion efficiency (IPCE) plot under electrolyte-side illumination (as shown in Figure 1a) in aqueous 0.5 M potassium phosphate solution that is buffered to pH 8. The electrochemical measurement was performed in a three-electrode configuration with the photoanode as the working electrode, a saturated calomel (SCE) reference electrode, and a Pt wire (0.8 mm^2 surface area) as the counter electrode, using a potentiostat

(Model SP-200, BioLogic). Potentials are reported versus RHE using V versus RHE (volt) = V versus SCE (volt) + [0.059 (volt) × pH] + 0.244 (volt). $J-V$ curves were measured at a scan rate of 50 mV/s under illumination from a class-AAA solar simulator (Model 94063A, Oriel) with the total intensity measured by a calibrated silicon solar cell and readout meter (Model 91150 V, Newport). Although it is common to simply use an overall illumination intensity of 100 mW/cm^2 for $J-V$ measurements, this can introduce errors because of the significant spectral mismatch between the AM 1.5G standard and the lamp output. Therefore, to ensure that the illumination closely simulates the AM 1.5G standard, we measured the spectral irradiance of the illumination at the sample location using a spectrometer (Ocean Optics) and adjusted the overall intensity to 85 mW/cm^2 to achieve the desired 7.5 mA/cm^2 integrated photon current up to the 515 nm band-edge wavelength of $BiVO_4$ (illumination spectrum at sample is provided and compared to AM 1.5G spectrum in Supporting Information Figure S4). IPCE was measured at 1.23 V versus RHE using a 75 W Xe lamp equipped with a monochromator (CM-110, 1/8 m, Spectra Products). The incident light intensity at each wavelength was measured by a calibrated silicon photodiode and is given in Supporting Information Figure S4. The IPCE was calculated from IPCE (%) = $[J_{ph}$ (mA/cm^2) × 1240 (volt × nm)]/$[P_{mono}$ (mW/cm^2) × λ (nm)] × 100%, where J_{ph} is the photocurrent density, P_{mono} is the intensity of the incident monochromatic light, and λ is the wavelength of the monochromatic light.[20] During all $J-V$ and IPCE measurements, the electrolyte was purged with Ar to remove dissolved oxygen and prevent signals from oxygen reduction.

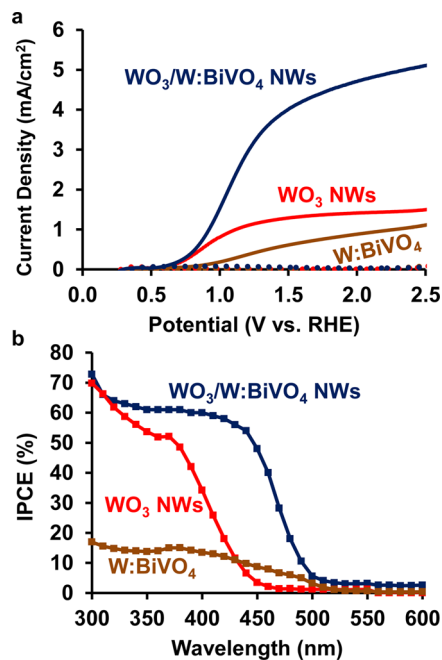The photocurrent of the WO_3/W:$BiVO_4$ core/shell NWs ($J-V$ curve in Figure 3a) reaches 3.1 mA/cm^2 at a potential of

Figure 3. Photoelectrochemical response of the WO_3/W:$BiVO_4$ NW photoanode and control samples in 0.5 M potassium phosphate electrolyte buffered to pH 8. (a) Current–voltage ($J-V$) curves (solid lines: simulated AM 1.5G illumination, dotted lines: dark) and (b) Incident photon-to-current efficiency (IPCE) measured at 1.23 V_{RHE}.

1.23 V versus RHE under the simulated AM 1.5G illumination and closely matches the photocurrent of 3.0 mA/cm^2 obtained by integrating the measured IPCE (Figure 3b) over the standard AM 1.5G spectrum. These photocurrent values of the WO$_3$/W:BiVO$_4$ NWs without the addition of OER catalysts are quite close to that achieved at the same potential by the best-performing W-gradient doped BiVO$_4$ photoanode with an OER catalyst added for which, although a value of 3.6 mA/cm^2 was reported at 1.23 V versus RHE under simulated illumination, a value of ∼3.4 mA/cm^2 is obtained by multiplying J_{max} (7.5 mA/cm^2) by the reported η_{abs} of 75% and the reported η_{sep} of 60% at 1.23 V versus RHE, even if η_{trans} = 100%.[18] Apart from that best-performing W-gradient doped BiVO$_4$ photoanode for which IPCE was not reported, the average IPCE of our WO$_3$/W:BiVO$_4$ core/shell NWs over the 300−450 nm range at 1.23 V versus RHE is about 60%, which is the highest for any BiVO$_4$-based photoanode at this potential, including those with added OER catalysts.[6,19,26,27,40,42,47]

To evaluate possible synergistic effects between WO$_3$ and W:BiVO$_4$ in the core/shell NWs, J−V curves (Figure 3a) and IPCEs (Figure 3b) were also measured for the bare WO$_3$ NW array and a porous 1.5 μm-thick 7% W-doped BiVO$_4$ film containing the same mass of Bi as that in the core/shell NWs (hereafter referred to as the 'same-mass W:BiVO$_4$ film', SEM images provided in Supporting Information Figure S2). 7% W-doping was chosen because it matches the average doping level in the W:BiVO$_4$ shell of the WO$_3$/W:BiVO$_4$ NWs. The same-mass W:BiVO$_4$ film was prepared by drop-casting a solution containing Bi:V:W = 100:93:7 onto bare FTO glass, with drop-casting and subsequent annealing steps identical to those used for the WO$_3$/W:BiVO$_4$ NWs. The W ions were obtained by dissolution of H$_2$WO$_4$ in 30% aqueous H$_2$O$_2$ followed by dilution in deionized water. As shown in Figure 3a, while the WO$_3$ NWs and same-mass W:BiVO$_4$ film separately generate photocurrents of 1.1 and 0.4 mA/cm^2 at 1.23 V versus RHE, respectively, the WO$_3$/W:BiVO$_4$ NWs generate a photocurrent of 3.1 mA/cm^2 at 1.23 V versus RHE, which is more than twice the sum of the separate photocurrents, indicating a powerful synergistic effect between the WO$_3$ core and the W:BiVO$_4$ shell. This synergy is also evident in the IPCE results (Figure 3b, measured at 1.23 V versus RHE). As will be described next, light in the 300−515 nm wavelength range is primarily absorbed in the W:BiVO$_4$ shell, since it is the outer material and a stronger light-absorber than WO$_3$. Nevertheless, the average IPCE of the WO$_3$/W:BiVO$_4$ NWs over the 300−450 nm wavelength range (∼60%) is more than four times higher than that of the same-mass W:BiVO$_4$ film (13%), and is similar to the maximum IPCE of the WO$_3$ NWs. This indicates that the WO$_3$ NWs are improving the collection efficiency of charges generated in W:BiVO$_4$, which is a synergistic effect. In other words, these IPCE results suggest that the WO$_3$/W:BiVO$_4$ core/shell NWs utilize the best properties of each component in that they absorb light like BiVO$_4$, and have charge transport properties similar to WO$_3$, as will be elaborated next.

Next, we determine the reasons for the excellent performance of the WO$_3$/W:BiVO$_4$ core/shell NWs by extracting the efficiencies of the subprocesses η_{abs}, η_{sep}, and η_{trans} and comparing them, as appropriate, to those of the bare WO$_3$ NWs and same-mass W:BiVO$_4$ film. The wavelength-dependent optical absorption properties of the samples were obtained with an integrating sphere using illumination from a Xe lamp coupled to a monochromator. For the absorption measure-

ments, the samples were placed in the center of the sphere, with light incident normal to the sample surface. For the reflectance measurements, the samples were aligned to a port at the backside of the integrating sphere and the reflectance spectra were normalized to the reflection of a white standard. A calibrated silicon photodiode at a second port was used to measure the unabsorbed and reflected light, respectively. First, the light absorption spectrum of the WO$_3$/W:BiVO$_4$ NWs (Figure 4a) closely resembles that of BiVO$_4$, with absorption onset at 515 nm (∼2.4 eV) and a smooth rise to nearly complete absorption at 450 nm. Since the bare WO$_3$ NWs hardly absorb any light at these wavelengths, the strong light absorption by the core/shell NWs, especially around 450 nm, indicates that light absorption occurs efficiently in the W:BiVO$_4$ shell despite the small W:BiVO$_4$ shell thickness of only 60 nm, which is far below the light absorption depth of about 250 nm at a wavelength of 450 nm.[19,53] This strong absorption can be attributed to the long path for light, which is equal to the NW length, through the W:BiVO$_4$ shell. Based on the strong absorption at these longer wavelengths and since it is the outer material, the W:BiVO$_4$ shell should absorb most of the light in the entire 300−515 nm wavelength range. Nevertheless, some light of wavelength shorter than 460 nm will also enter the WO$_3$ NW cores through their tips where the W:BiVO$_4$ coating is very thin, and be absorbed by WO$_3$. Moreover, η_{abs} of the WO$_3$/W:BiVO$_4$ NWs, when the absorption is integrated over the AM 1.5G spectrum, is 69%, which is slightly higher than the 66% η_{abs} of the 1.5 μm-thick porous same-mass W:BiVO$_4$ film due to reduced reflection by the NWs (Supporting Information Figure S5). Nevertheless, the light absorption enhancement is much smaller than the over 4-fold IPCE enhancement between the WO$_3$/W:BiVO$_4$ NWs and same-mass W:BiVO$_4$ film, indicating that light absorption is not the main reason for the difference in performance of these photoanodes.

The charge separation and surface transfer efficiencies η_{sep} and η_{trans} are determined by adding a fast hole scavenger to the electrolyte.[4,21] Specifically, J−V curves were measured with 0.5 M H$_2$O$_2$ added to the 0.5 M potassium phosphate electrolyte as a hole scavenger. Since the rate of charge transfer to the electrolyte by oxidation of H$_2$O$_2$ at the semiconductor/electrolyte interface is very fast, it can be assumed that the surface recombination of charges is eliminated and $\eta_{trans}(H_2O_2)$ ≈ 100%.[13,19] While the H$_2$O oxidation photocurrent is given by $J_{H_2O} = J_{max} \times \eta_{abs} \times \eta_{sep} \times \eta_{trans}$, the H$_2O_2$ oxidation photocurrent is given by $J_{H_2O_2} \approx J_{max} \times \eta_{abs} \times \eta_{sep}$. Since the addition of H$_2$O$_2$ did not change the light absorption, pH or flat band potentials of the photoanodes, and the saturated photocurrents for H$_2$O and H$_2$O$_2$ oxidation were the same for each electrode, indicating that no current doubling occurs in the presence of H$_2$O$_2$, J_{max}, η_{abs} and η_{sep} are the same for $J_{H_2O_2}$ and J_{H_2O}.[13,19] As shown in Figure 4b, when H$_2$O$_2$ is added to the electrolyte, the WO$_3$/W:BiVO$_4$ NWs generate a photocurrent nearly equal to 4.0 mA/cm^2 at 1.23 V versus RHE under precisely simulated AM 1.5G illumination, indicating that the $\eta_{abs} \times \eta_{sep}$ (=$J_{H_2O_2}/J_{max}$) product equals 53%, which is the highest value for any reported BiVO$_4$-based photoanode. The photocurrent onset at around 0.45 V versus RHE is close to the flat band potential of WO$_3$ (∼0.4 V versus RHE[41]), as expected. Importantly, these high photocurrents at potentials below 1.23 V versus RHE could be achieved for H$_2$O oxidation by the addition of OER catalysts. Such a photoanode would then be
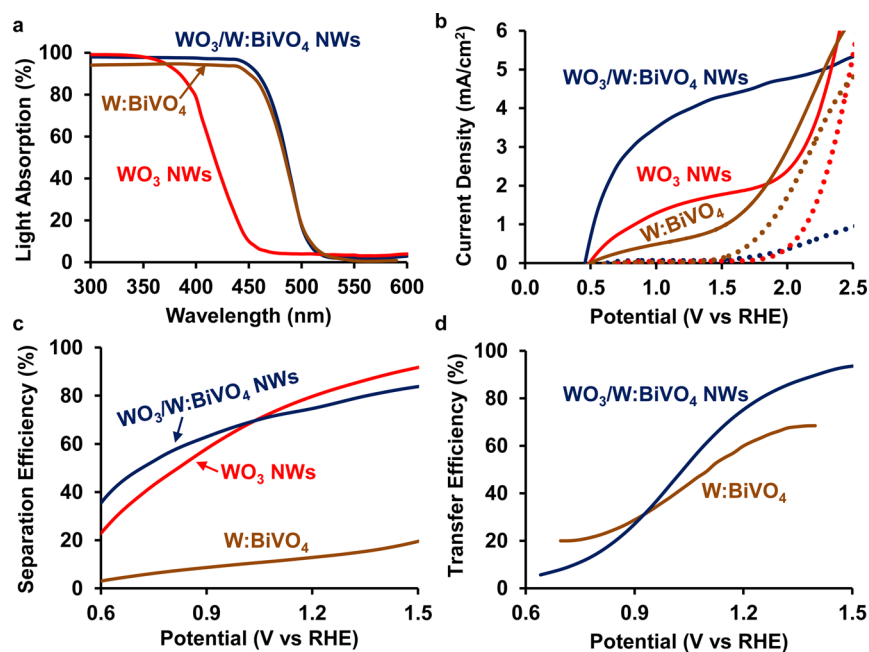
Figure 4. Efficiencies of subprocesses that comprise the overall photoelectrochemical response of the $WO_3/W:BiVO_4$ NW photoanode and control samples. (a) Light absorption efficiency (η_{abs}) and (b) J–V curve under simulated AM 1.5G illumination with H_2O_2 added to the potassium phosphate electrolyte as a hole scavenger, which demonstrates the photocurrent achieved when the surface charge transfer efficiency is nearly 100%. (c) Charge separation (η_{sep}) and (d) surface charge transfer efficiency (η_{trans}) of the $WO_3/W:BiVO_4$ NWs and, where appropriate, the bare WO_3 NWs and same-mass $W:BiVO_4$ film.

extremely promising for PEC water-splitting with a tandem photocathode which would supply the necessary bias and perform H_2O reduction.

Moreover, the charge separation and surface transfer efficiencies can be individually calculated as $\eta_{sep} \approx J_{H_2O_2}/(J_{max} \times \eta_{abs})$ and $\eta_{trans} \approx J_{H_2O}/J_{H_2O_2}$, and are plotted in Figure 4c and d, respectively. The η_{trans} of the $WO_3/W:BiVO_4$ NWs (78%) is higher than that of the porous same-mass $W:BiVO_4$ film (62%) at 1.23 V versus RHE, perhaps indicating that the surface area of the NWs is higher than that of the porous film. However, this is not sufficient to explain the nearly 8 times higher photocurrent of the $WO_3/W:BiVO_4$ NWs at 1.23 V versus RHE, which means that the improvement must primarily come from increased η_{sep}. As expected, charge separation in the same-mass 1.5 μm thick polycrystalline $W:BiVO_4$ (13% at 1.23 V versus RHE) is extremely poor due to strong bulk recombination, since the average particle radius of 250 nm is larger than the hole diffusion length in $W:BiVO_4$ (70–100 nm[19,54,55]) and the film thickness is much larger than the 300 nm electron diffusion length.[6] On the other hand, charge separation in the $WO_3/W:BiVO_4$ NWs (77% at 1.23 V versus RHE) is relatively more efficient.

Next, we examine the reasons for the high charge separation efficiency of the $WO_3/W:BiVO_4$ core/shell NWs. Charges are generated mostly by light absorption in the $W:BiVO_4$ shell and to a smaller extent by light absorption in the WO_3 NW cores. First, considering charges generated in the 60 nm thick $W:BiVO_4$ shell, holes can readily reach the semiconductor/ electrolyte interface because they only need to travel a short distance that is less than the reported hole diffusion length (70–100 nm[19,54,55]) in W-doped $BiVO_4$. Holes generated in the $W:BiVO_4$ shell also have a low probability of reaching and recombining at defect states at the FTO/semiconductor interface[25,37] because WO_3, due to its lower-lying valence

band, serves as a "hole mirror". For electrons, their diffusion lengths in $W:BiVO_4$ and WO_3 are ~300 nm[6] and ~500 nm,[56] respectively, which are shorter than the length of the NWs, so the electron transport to the current collector will rely on drift and hence prefer the high electrical conductivity pathway. The axial electron conductivity of the WO_3 NWs (I–V curve and experimental details in Supporting Information Figure S6) is determined to be on the order of 1 S/cm, which is much higher than that of the 7% $W:BiVO_4$ film (10^{-8} S/cm) estimated by an impedance measurement (Nyquist plot and experimental details in Supporting Information Figure S7). Hence, electrons generated in the $W:BiVO_4$ shell will first travel radially inward to the WO_3 cores, and then travel to the current collector through WO_3. In addition, apart from the small thickness of the $W:BiVO_4$ shell, the electric fields due to the gradient W-doping[18] and the staggered type-II $WO_3/W:BiVO_4$ hetero-junction[41,46] also significantly improve η_{sep} as evidenced by the fact that η_{sep} in an undoped $BiVO_4$ layer of similar thickness was reported to be only 20% at 1.23 V versus RHE.[25] Second, as seen by comparing to η_{sep} of the bare WO_3 NWs (Figure 4c), charges generated in the 75 nm diameter WO_3 NW cores also have high η_{sep}. Holes can readily reach the electrolyte by first transferring to $W:BiVO_4$ across the $WO_3/W:BiVO_4$ hetero-junction since the NW diameter is smaller than the hole diffusion length of ~150 nm.[57] Electrons can reach the current collector directly and efficiently because of the high electrical conductivity of WO_3. Therefore, as a result of efficient charge separation in both the core and shell, the charge separation efficiency in the $WO_3/W:BiVO_4$ core/shell NWs is much higher than that in the same-mass $W:BiVO_4$ film.

Compared to the recent top-performer, a 200 nm thick gradient-doped compact $W:BiVO_4$ film synthesized on a textured substrate that achieved $\eta_{abs} \approx 75\%$ and $\eta_{sep} \approx 60\%$ at 1.23 V versus RHE,[18] the η_{abs} of the present $WO_3/W:BiVO_4$ NWs (69%) is very similar despite the small $BiVO_4$ thickness of

60 nm due to the long optical path for light absorption along the NW length. At the same time, η_{sep} of the present $WO_3/$W:$BiVO_4$ NWs (77%) is significantly higher due to the small $BiVO_4$ thickness (60 nm versus 200 nm), and the presence of the conductive WO_3 NW pathway for electron transport. The efficiency of the present $WO_3/$W:$BiVO_4$ NW photoanodes is also higher than that of a previously reported $WO_3/BiVO_4$ core/shell nanorod photoanode[46] and a WO_3 NW/$BiVO_4$ heterojunction photoanode,[47] for a number of reasons. In the case of the previously reported $WO_3/BiVO_4$ core/shell nanorods,[46] a thin $BiVO_4$ layer was deposited onto short (500−1000 nm) WO_3 nanorods that had a hexagonal crystal structure. In the present study, we synthesize longer (2.5 μm) WO_3 NWs with a higher surface area, which permits a higher $BiVO_4$ loading and therefore higher light absorption, and with a monoclinic WO_3 crystal structure which results in faster electron transport compared to the hexagonal structure, therefore allowing more efficient charge separation. In the case of the previously reported WO_3 NW/$BiVO_4$ heterojunction, which achieved a photocurrent density of ∼2.5 mA/cm^2 at 1.23 V versus RHE under simulated AM 1.5G illumination when coated with an OER catalyst and ∼2.1 mA/cm^2 without the OER catalyst,[47] a 1 μm-thick layer of porous $BiVO_4$ was deposited on top of a 1 μm-thick porous WO_3 film which was composed of multiple layers of urchin-like structures consisting of short (<600 nm length) WO_3 NWs. The charge separation efficiency in the present $WO_3/$W:$BiVO_4$ NWs is expected to be much higher than in this heterojunction film because of the much smaller $BiVO_4$ thickness and the presence of continuous WO_3 NW crystals (rather than multiple layers of shorter NWs) that directly conduct electrons to the substrate.

Lastly, the stability of the $WO_3/$W:$BiVO_4$ core/shell NWs and their faradaic efficiency for water oxidation were evaluated in a three-electrode configuration with the photoanode (∼1 cm^2 masked area) as the working electrode, a Ag/AgCl (1 M KCl) reference electrode, and a Pt wire as the counter electrode. The potential of the photoanode was determined using V versus RHE (volt) = V versus Ag/AgCl (volt) + [0.059 (volt) × pH] + 0.236 (volt). The experiment was conducted in a sealed cell containing 0.5 M Na_2SO_4 electrolyte (pH ∼ 6) through which He carrier gas was flowed at a rate of 5 sccm. After purging the electrolyte of dissolved oxygen, the potential of the photoanode was held at 1.23 V versus RHE under simulated AM 1.5G illumination using a potentiostat, and both the photocurrent and the oxygen gas concentration in the He carrier were monitored (Figure 5). The concentration of

oxygen in the He carrier, as measured by gas chromatography (SRI Instruments), increased and then reached a steady value at around 30 min once the dissolved oxygen content in the electrolyte reached a steady value. Bubbles were continuously evolved from the photoanode, and the accumulation and release of these bubbles led to the observed variations in photocurrent over the duration of the measurement. The photocurrent of the $WO_3/$W:$BiVO_4$ NWs remained at approximately 3.1 mA/cm^2 over 1 h without degradation, and the faradaic efficiency for water oxidation to O_2 was found to be 79%. This result shows that the $WO_3/$W:$BiVO_4$ NWs are stable and are indeed oxidizing water into O_2.

In conclusion, the critical advance in this work is the use of an electrically conductive WO_3 NW array to overcome the intrinsically poor charge transport properties of $BiVO_4$ without compromising light absorption, thereby achieving η_{abs} of 69% and η_{sep} of 77% at 1.23 V versus RHE, for a combined $\eta_{abs} \times \eta_{sep}$ product of 53% which, to the best of our knowledge, is the highest achieved to date in any $BiVO_4$-based photoanode (compared to the highest 45% previously reported[18]). Even without any OER catalysts, these core/shell NWs achieve a photocurrent of 3.1 mA/cm^2 at 1.23 V versus RHE under precisely simulated AM 1.5G illumination, which is quite close to the photocurrent achieved at the same potential by the best-performing $BiVO_4$-based photoanode with OER catalysts. If the surface charge transfer efficiency of these core/shell NWs could be improved from 79 to 100% by adding OER catalysts, they would achieve a photocurrent of nearly 4.0 mA/cm^2 at 1.23 V versus RHE. Importantly, the $WO_3/$W:$BiVO_4$ NWs were synthesized from economical precursors in an inexpensive and scalable manner. These promising results bring us a step closer to efficient photoanodes for tandem PEC water-splitting systems.

■ ASSOCIATED CONTENT

Ⓢ Supporting Information

Additional SEM images, histograms of nanowire dimensions, more detailed X-ray diffraction data, illumination spectra, reflectance spectra, and raw data from which conductivities were extracted. This material is available free of charge via the Internet at http://pubs.acs.org.

■ AUTHOR INFORMATION

Corresponding Author

*E-mail: xlzheng@stanford.edu. Fax: (650) 723-1748.

Present Address

∥(P.M.R.) Department of Mechanical Engineering Worcester Polytechnic Institute, Worcester, MA 01609. E-mail: pmrao@wpi.edu.

Author Contributions

⊥P.M.R. and L.C. contributed equally.

P.M.R. and L.C. carried out the photoanode synthesis and characterization. P.M.R., L.C., and X.Z. conceived the study and wrote the manuscript. C.L. measured the stability and faradaic efficiency of the photoanodes and participated in revision of the manuscript. I.S.C. assisted in preparation of reagents for the synthesis and in the electrochemical characterization and participated in revision of the manuscript. C.H.L. performed the single-nanowire conductivity measurements. J.M.W. performed the thin film impedance measurements. All authors have commented on the manuscript.
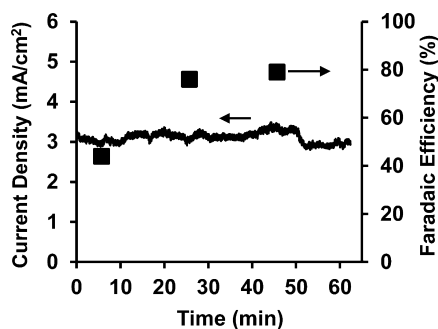

Figure 5. Stability and faradaic efficiency of the $WO_3/$W:$BiVO_4$ NW photoanode in 0.5 M Na_2SO_4 under simulated AM 1.5G illumination.

■ REFERENCES

(1) Bensaid, S.; Centi, G.; Garrone, E.; Perathoner, S.; Saracco, G. *ChemSusChem* **2012**, *5*, 500−521.

(2) Prévot, M. S.; Sivula, K. *J. Phys. Chem. C* **2013**, *117*, 17879−17893.

(3) Hu, S.; Xiang, C. X.; Haussener, S.; Berger, A. D.; Lewis, N. S. *Energy Environ. Sci.* **2013**, *6*, 2984−2993.

(4) Liu, C.; Tang, J.; Chen, H. M.; Liu, B.; Yang, P. *Nano Lett.* **2013**, *13*, 2989−2992.

(5) Liu, C.; Dasgupta, N. P.; Yang, P. *Chem. Mater.* **2013**, DOI: 10.1021/cm4023198.

(6) Seabold, J.; Zhu, K.; Neale, N. R. *Phys. Chem. Chem. Phys.* **2013**, *16*, 1121−1131.

(7) Park, H. S.; Lee, H. C.; Leonard, K. C.; Liu, G. J.; Bard, A. J. *ChemPhysChem* **2013**, *14*, 2277−2287.

(8) Woodhouse, M.; Parkinson, B. A. *Chem. Soc. Rev.* **2009**, *38*, 197−210.

(9) Bin-Daar, G.; Dare-Edwards, M. P.; Goodenough, J. B.; Hamnett, A. *J. Chem. Soc., Faraday Trans. 1* **1983**, *79*, 1199−1213.

(10) Cho, I. S.; Lee, C. H.; Feng, Y.; Logar, M.; Rao, P. M.; Cai, L.; Kim, D. R.; Sinclair, R.; Zheng, X. *Nat. Commun.* **2013**, *4*, 1723.

(11) Cho, I. S.; Chen, Z.; Forman, A. J.; Kim, D. R.; Rao, P. M.; Jaramillo, T. F.; Zheng, X. *Nano Lett.* **2011**, *11*, 4978−4984.

(12) Gaillard, N.; Cole, B.; Kaneshiro, J.; Miller, E. L.; Marsen, B.; Weinhardt, L.; Baer, M.; Heske, C.; Ahn, K.-S.; Yan, Y.; Al-Jassim, M. M. *J. Mater. Res.* **2010**, *25*, 45−51.

(13) Dotan, H.; Sivula, K.; Graetzel, M.; Rothschild, A.; Warren, S. C. *Energy Environ. Sci.* **2011**, *4*, 958−964.

(14) Wang, G.; Ling, Y.; Wheeler, D. A.; George, K. E. N.; Horsley, K.; Heske, C.; Zhang, J. Z.; Li, Y. *Nano Lett.* **2011**, *11*, 3503−3509.

(15) Zhong, D. K.; Cornuz, M.; Sivula, K.; Graetzel, M.; Gamelin, D. R. *Energy Environ. Sci.* **2011**, *4*, 1759−1764.

(16) Kay, A.; Cesar, I.; Graetzel, M. *J. Am. Chem. Soc.* **2006**, *128*, 15714−15721.

(17) Park, Y.; McDonald, K. J.; Choi, K.-S. *Chem. Soc. Rev.* **2013**, *42*, 2321−2337.

(18) Abdi, F. F.; Han, L.; Smets, A. H. M.; Zeman, M.; Dam, B.; van de Krol, R. *Nat. Commun.* **2013**, *4*, 2195.

(19) Zhong, D. K.; Choi, S.; Gamelin, D. R. *J. Am. Chem. Soc.* **2011**, *133*, 18370−18377.

(20) Chen, Z.; Jaramillo, T. F.; Deutsch, T. G.; Kleiman-Shwarscstein, A.; Forman, A. J.; Gaillard, N.; Garland, R.; Takanabe, K.; Heske, C.; Sunkara, M.; McFarland, E. W.; Domen, K.; Miller, E. L.; Turner, J. A.; Dinh, H. N. *J. Mater. Res.* **2010**, *25*, 3−16.

(21) Seabold, J. A.; Choi, K. S. *J. Am. Chem. Soc.* **2012**, *134*, 2186−2192.

(22) Pilli, S. K.; Furtak, T. E.; Brown, L. D.; Deutsch, T. G.; Turner, J. A.; Herring, A. M. *Energy Environ. Sci.* **2011**, *4*, 5028−5034.

(23) Jeon, T. H.; Choi, W.; Park, H. *Phys. Chem. Chem. Phys.* **2011**, *13*, 21392−21401.

(24) McDonald, K. J.; Choi, K. S. *Energy Environ. Sci.* **2012**, *5*, 8553−8557.

(25) Abdi, F. F.; van de Krol, R. *J. Phys. Chem. C* **2012**, *116*, 9398−9404.

(26) Jia, Q. X.; Iwashina, K.; Kudo, A. *Proc. Natl. Acad. Sci. U.S.A.* **2012**, *109*, 11564−11569.

(27) Luo, W.; Yang, Z.; Li, Z.; Zhang, J.; Liu, J.; Zhao, Z.; Wang, Z.; Yan, S.; Yu, T.; Zou, Z. *Energy Environ. Sci.* **2011**, *4*, 4046−4051.

(28) Choi, S. K.; Choi, W.; Park, H. *Phys. Chem. Chem. Phys.* **2013**, *15*, 6499−6507.

(29) Ding, C. M.; Shi, J. Y.; Wang, D. G.; Wang, Z. J.; Wang, N.; Liu, G. J.; Xiong, F. Q.; Li, C. *Phys. Chem. Chem. Phys.* **2013**, *15*, 4589−4595.

(30) Sayama, K.; Nomura, A.; Arai, T.; Sugita, T.; Abe, R.; Yanagida, M.; Oi, T.; Iwasaki, Y.; Abe, Y.; Sugihara, H. *J. Phys. Chem. B* **2006**, *110*, 11352−11360.

(31) Berglund, S. P.; Flaherty, D. W.; Hahn, N. T.; Bard, A. J.; Mullins, C. B. *J. Phys. Chem. C* **2011**, *115*, 3794−3802.

(32) Park, H. S.; Kweon, K. E.; Ye, H.; Paek, E.; Hwang, G. S.; Bard, A. J. *J. Phys. Chem. C* **2011**, *115*, 17870−17879.

(33) Berglund, S. P.; Rettie, A. J. E.; Hoang, S.; Mullins, C. B. *Phys. Chem. Chem. Phys.* **2012**, *14*, 7065−7075.

(34) Luo, W. J.; Wang, J. J.; Zhao, X.; Zhao, Z. Y.; Li, Z. S.; Zou, Z. G. *Phys. Chem. Chem. Phys.* **2013**, *15*, 1006−1013.

(35) Jeong, H. W.; Jeon, T. H.; Jang, J. S.; Choi, W.; Park, H. *J. Phys. Chem. C* **2013**, *117*, 9104−9112.

(36) Abdi, F. F.; Firet, N.; van de Krol, R. *ChemCatChem* **2013**, *5*, 490−496.

(37) Liang, Y.; Tsubota, T.; Mooij, L. P. A.; van de Krol, R. *J. Phys. Chem. C* **2011**, *115*, 17594−17598.

(38) Chatchai, P.; Murakami, Y.; Kishioka, S. y.; Nosaka, A. Y.; Nosaka, Y. *Electrochem. Solid-State Lett.* **2008**, *11*, H160−H163.

(39) Pilli, S. K.; Deutsch, T. G.; Furtak, T. E.; Turner, J. A.; Brown, L. D.; Herring, A. M. *Phys. Chem. Chem. Phys.* **2012**, *14*, 7032−7039.

(40) Saito, R.; Miseki, Y.; Sayama, K. *Chem. Commun. (Cambridge, U.K.)* **2012**, *48*, 3833−3835.

(41) Hong, S.; Lee, S.; Jang, J. S.; Lee, J. S. *Energy Environ. Sci.* **2011**, *4*, 1781−1787.

(42) Zhang, K.; Shi, X. J.; Kim, J. K.; Park, J. H. *Phys. Chem. Chem. Phys.* **2012**, *14*, 11119−11124.

(43) Ng, Y. H.; Iwase, A.; Kudo, A.; Amal, R. *J. Phys. Chem. Lett.* **2010**, *1*, 2607−2612.

(44) Pilli, S. K.; Deutsch, T. G.; Furtak, T. E.; Brown, L. D.; Turner, J. A.; Herring, A. M. *Phys. Chem. Chem. Phys.* **2013**, *15*, 3273−3278.

(45) Jiang, J.; Wang, M.; Li, R.; Ma, L.; Guo, L. *Int. J. Hydrogen Energy* **2013**, *38*, 13069−13076.

(46) Su, J.; Guo, L.; Bao, N.; Grimes, C. A. *Nano Lett.* **2011**, *11*, 1928−1933.

(47) Pilli, S. K.; Janarthanan, R.; Deutsch, T. G.; Furtak, T. E.; Brown, L. D.; Turner, J. A.; Herring, A. M. *Phys. Chem. Chem. Phys.* **2013**, *15*, 14723−14728.

(48) Hou, Y.; Zuo, F.; Dagg, A.; Feng, P. *Nano Lett.* **2012**, *12*, 6464−6473.

(49) Rao, P. M.; Cho, I. S.; Zheng, X. *Proc. Combust. Inst.* **2013**, *34*, 2187−2195.

(50) Rao, P. M.; Zheng, X. *Nano Lett.* **2011**, *11*, 2390−2395.

(51) Cai, L. L.; Rao, P. M.; Zheng, X. *Nano Lett.* **2011**, *11*, 872−877.

(52) Rao, P. M.; Zheng, X. *Proc. Combust. Inst.* **2011**, *33*, 1891−1898.

(53) Zhao, Z.; Li, Z.; Zou, Z. *Phys. Chem. Chem. Phys.* **2011**, *13*, 4746−4753.

(54) Abdi, F. F.; Savenije, T. J.; May, M. M.; Dam, B.; van de Krol, R. *J. Phys. Chem. Lett.* **2013**, *4*, 2752−2757.

(55) Rettie, A. J. E.; Lee, H. C.; Marshall, L. G.; Lin, J. F.; Capan, C.; Lindemuth, J.; McCloy, J. S.; Zhou, J. S.; Bard, A. J.; Mullins, C. B. *J. Am. Chem. Soc.* **2013**, *135*, 11389−11396.

(56) Butler, M. A. *J. Appl. Phys.* **1977**, *48*, 1914−1920.

(57) Santato, C.; Ulmann, M.; Augustynski, J. *Adv. Mater. (Weinheim, Germany)* **2001**, *13*, 511−514.